

A Tale of Two Grains: impact of grain size on ring formation via nonideal MHD processes

XIAO HU (胡晓),¹ LILE WANG (王力乐),² SATOSHI OKUZUMI (奥住聡),³ AND ZHAOHUAN ZHU (朱照寰)¹

¹*Department of Physics and Astronomy, University of Nevada, Las Vegas, 4505 South Maryland Parkway, Las Vegas, NV 89154*

²*Center for Computational Astrophysics, Flatiron Institute, New York, NY 10010; lwang@flatironinstitute.org*

³*Department of Earth and Planetary Sciences, Tokyo Institute of Technology, Meguro, Tokyo, 152-8551, Japan*

ABSTRACT

Substructures in PPDs, whose ubiquity was unveiled by recent ALMA observations, are widely discussed regarding their possible origins. We carry out global full magnetohydrodynamic (MHD) simulations in axisymmetry, coupled with self-consistent ray-tracing radiative transfer, thermochemistry, and non-ideal MHD diffusivities. The abundance profiles of grains are also calculated based on the global dust evolution calculation, including sintering effects. We found that dust size plays a crucial role in the ring formation around the snowlines of protoplanetary disks (PPDs) through the accretion process. Disk ionization structures and thus tensorial conductivities depend on the size of grains. When grains are significantly larger than PAHs, the non-ideal MHD conductivities change dramatically across each snow line of major volatiles, leading to a sudden change of the accretion process across the snow lines and the subsequent formation of gaseous rings/gaps there. On the other hand, the variations of conductivities are a lot less with only PAH sized grains in disks and then these disks retain smoother radial density profiles across snow lines.

Keywords: accretion, accretion disks — magnetohydrodynamics (MHD) — planets and satellites: formation — circumstellar matter — method: numerical

1. INTRODUCTION

Studying the dynamics of protoplanetary disks is crucial for not only constructing comprehensive planet formation theory, but also understanding the fine features in recent high resolution observations. The *2014 ALMA campaign* provided unprecedented details of the HL Tau disk (ALMA Partnership et al. 2015). Patterns that are broadly axisymmetric, such as multiple bright and dark rings in dust continuum emission, are found to be common in protoplanetary disks in subsequent observations (e.g. Huang et al. 2018; Long et al. 2018).

Recent MHD simulations suggest that substructure formation can be achieved by non-ideal MHD processes, including Ohmic resistivity and ambipolar diffusion. Processes like redistribution of magnetic flux, direct feeding of avalanche accretion, and midplane magnetic reconnection (Suriano et al. 2017, 2018, 2019) can alter disk surface density. Meanwhile, snow lines modify dust drift, growth, and fragmentation, causing surface density variation radially (Zhang et al. 2015; Okuzumi et al. 2016). The abundance of dust is an important factor for disk’s ionization, affecting the coupling between gas and magnetic fields (e.g., Wardle 2007; Bai 2011a). Near snow lines, we can expect the feedback

from dust to non-ideal MHD, then to disk accretion itself. In Hu et al. (2019), this idea was tested by incorporating snow line induced dust distribution and ionization change into MHD disk simulations. The ionization structure was pre-calculated with dust distribution from global dust evolution including sintering effects (Okuzumi et al. 2016). The ionization structure and the non-ideal MHD diffusivities have sharp changes at the snow lines due to the change of dust size there. This leads to a discontinuous accretion flow across the snow lines. With time, such a discontinuous accretion flow naturally produces gaps and adjacent rings at CO₂ and C₂H₆ snow lines. This dust-to-gas feedback requires much less dust to take effect, compared to hydrodynamic drag mechanism (e.g., Gonzalez et al. 2017).

However, the simple treatment of dust on magnetic diffusion is also one of the major caveats of current non-ideal MHD simulations. Grain-modified magnetic diffusivities in protoplanetary disks were first explored in the very small grain limit (\sim nm size, or PAH scale). They are known for substantially reducing the level of ionization, killing magnetorotational instability (MRI) (Bai 2011a; Wang et al. 2018). Charged grains, when very small, can be regarded as heavy ions in diffusion calculations, while its geometric size starts to take effect in

larger (sub-micron to micron-sized) grains. Xu & Bai (2016) systematically explored the dependence of magnetic diffusivities on magnetic field strength with various grain sizes, and found the dependence of magnetic diffusion onto field strength shifts over grain sizes.

Another major caveat of most global MHD simulations is the uncertain disk temperature at the disk surface. Usually, a fixed or fast relaxation temperature profile is employed, and the initial density structure is derived based on hydrostatic equilibrium in R - z plane. The transition between the hot atmosphere (also referred to as corona) and the cold, dense disk is either sharp (e.g., Suriano et al. 2017, 2018, 2019) or with some artificial smooth profile (e.g., Hu et al. 2019; Béthune et al. 2017; Bai & Stone 2017).

In this work, we aim to overcome these two shortcomings by utilizing non-ideal MHD simulation with self-consistent thermochemistry and radiative transfer (Wang & Goodman 2017; Wang et al. 2018). The dust structure from global dust evolution is input into the simulations, while Ohmic resistivity and ambipolar diffusion profile can be obtained in real-time based on the ionization structure from the thermochemistry calculations. This letter is organized as follows. §2 briefly described the global dust evolution model and discussed the different roles between small and large grains in magnetic diffusion. §3 summarizes the numerical methods and parameter choices for our simulations. §4 presents diagnostics of disk radial and vertical structures, focusing on relating chemistry to ionization and at last accretion. We summarize the paper in §5.

2. DUST GRAINS AND DIFFUSION OF FIELDS

Similar to Hu et al. (2019), we use the radial profiles of dust surface density and particle size derived from a one-dimensional global dust evolution model having multiple snow lines by Okuzumi & Tazaki (2019). In this model, the grain size distribution follows a power-law with minimum and maximum grain sizes $a_{\text{gr,min}}$ and $a_{\text{gr,max}}$, respectively. The power law is such that the vertically integrated number density of grains per unit grain radius a_{gr} is proportional to $a_{\text{gr}}^{-3.5}$. We fixed the minimum grain size $a_{\text{gr,min}}$ as $0.1 \mu\text{m}$, whereas the maximum size $a_{\text{gr,max}}$ and total dust surface density Σ_d are evolved by computing radial drift and collisional growth/fragmentation. The calculation takes into account the low stickiness of CO_2 ice (Okuzumi & Tazaki 2019) and aggregate sintering (Okuzumi et al. 2016). In this 1-D dust evolutionary model, the fragmentation threshold velocity in regions where aggregate sintering takes place is chosen to be 40% of the threshold for unsintered aggregates. We assume a disk of weak gas turbulence with velocity dispersion of

1.7% of the sound speed. The gas surface density distribution for the dust evolution calculation is fixed in time and assumed to scale as R^{-1} , where R is the distance from the central star, at $R < 150 \text{ AU}$. We evolve the dust disk for 1.3 Myr, until the computed total millimeter fluxes from the dust disk match the ALMA observations of the HL Tau disk (ALMA Partnership et al. 2015).

The profile of Σ_d is plotted in the upper panel of Figure 1 (also shown in the left, second bottom panel in Figure 3 of Okuzumi & Tazaki 2019). Because of sintering, dust particles behind the snowlines CO_2 , C_2H_6 , and CH_4 (located at $R = 13, 29$, and 82 AU , respectively) experience enhanced collisional fragmentation and pile up there. Collisional fragmentation is also enhanced interior to the H_2O snow line (located at 4 AU) due to lack of water ice and results in another traffic jam of dust in this region.

The adopted dust's total geometric cross-section for chemistry calculation is plotted in the lower panel of Figure 1. Multiplying average cross-section of grains of all sizes and total dust abundance (number density over Hydrogen nucleus) we get dust's total geometric cross-section per Hydrogen nucleus. This number quantifies the contribution of dust particles to the whole chemical network. We make it unchanged in different models that are to be presented below. Note that we enhanced $\sigma_{\text{gr}}/\text{H}$ when $R < 4 \text{ AU}$, to ensure a moderate ionization fraction at inner disk.

In a weakly ionized protoplanetary disk, the equation of motion for charged species (whose inertia is usually negligible, see e.g. Xu & Bai 2016) is set by the equilibrium between the Lorentz force and the collision with neutrals,

$$Z_j e \left(\mathbf{E}' + \frac{\mathbf{v}_j}{c} \times \mathbf{B} \right) = \gamma_j \rho m_j \mathbf{v}_j \quad (1)$$

where for the charged species indicated by j , Z_j is its charge number (in unit charge e), m_j is its mass, \mathbf{v}_j is its drift velocity relative to the neutral background, $\gamma_j \equiv \langle \sigma v \rangle / (m + m_j)$ (m is the averaged particle mass of the neutrals) and $\langle \sigma v \rangle_j$ is its rate coefficient of momentum transfer with neutrals. The electric field in the frame comoving with the neutrals is denoted by \mathbf{E}' .

In the case of very tiny grains, the interaction between charged grains and neutral molecules are mediated by electric field from induced electric dipoles in the neutrals. This r^{-4} electric potential makes the collision rate coefficient $\langle \sigma v \rangle_j$ independent of temperature (e.g., Draine 2011). When grains get larger, their geometric cross section dominates their interactions with neutrals. This transition brought by the grain size is reflected by the Hall parameter, which is the ratio between the gy-

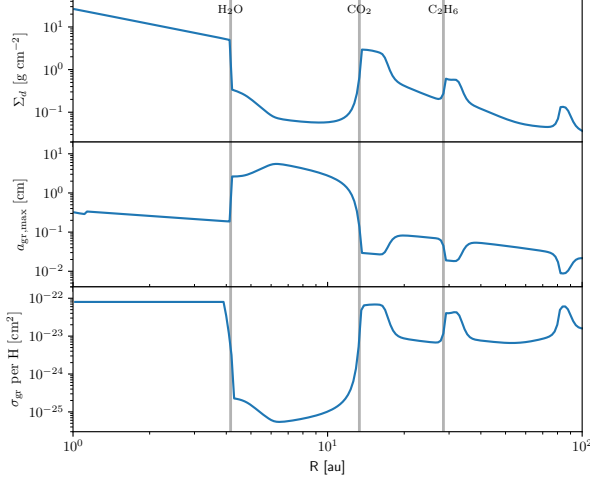


Figure 1. The upper and middle panels show the total dust surface density and maximum grain size, respectively, as a function of the distance R from the central star. The lower panel shows dust's total geometric cross-section per Hydrogen nucleus. Gray vertical lines indicate location of three snow lines. Note the traffic jam interior to the H_2O snow line is caused by the low stickiness of silicates, unrelated to sintering. The H_2O sintering zone corresponds to the small hill (at $R=4-6$ AU) at the bottom of the large gap in the Σ_d profile.

rofrequency of charged species under Lorentz force and their collision frequency with the neutrals:

$$\beta_j = \frac{|Z_j|eB}{m_j c} \frac{1}{\gamma_j \rho} \quad (2)$$

In our simulation, we adopt the recipes in Bai (2011b, 2014) to calculate collision coefficients between charged grains and neutrals:

$$\langle \sigma v \rangle_{\text{gr}} = \max \left[1.3 \times 10^{-9} |Z_{\text{gr}}|, 4 \times 10^{-3} \left(\frac{a_{\text{gr}}}{1 \mu\text{m}} \right)^2 \left(\frac{T}{100\text{K}} \right)^{1/2} \right] \text{cm}^3 \text{s}^{-1} \quad (3)$$

So the transition from electric potential dominated cross section to geometric cross section is at $\sim nm$ scale. Given $T=100\text{K}$, any single charged grain with $a_{\text{gr}} > 5.7 \times 10^{-8}$ cm needs to consider geometric effect when calculating collision coefficient. This difference is shown in the Ohmic, Hall and Pederson conductivities:

$$\begin{aligned} \sigma_O &= \frac{ec}{B} \sum_j n_j |Z_j| \beta_j, \\ \sigma_H &= \frac{ec}{B} \sum_j \frac{n_j Z_j}{1 + \beta_j^2}, \\ \sigma_P &= \frac{ec}{B} \sum_j \frac{n_j |Z_j| \beta_j}{1 + \beta_j^2}. \end{aligned} \quad (4)$$

Here the summation index j runs through all charged species, with n_j indicating the number density and charge of individual charged species. Since $\beta_{gr}, \beta_i \ll 1$ stands true throughout most regions of our disk, the difference between ions and grains is negligible for Hall conductivity σ_H . For Ohmic and Pederson conductivities, the contribution of larger grains can be orders of magnitude smaller than very small grains and ions. Using these conductivities, the general expressions for the three magnetic diffusivities are (Bai 2011b; Wang et al. 2018).

$$\begin{aligned} \eta_O &= \frac{c^2}{4\pi} \frac{1}{\sigma_O}, \quad \eta_H = \frac{c^2}{4\pi} \frac{\sigma_H}{\sigma_H^2 + \sigma_P^2}, \\ \eta_A &= \frac{c^2}{4\pi} \frac{\sigma_P}{\sigma_H^2 + \sigma_P^2} - \eta_O, \end{aligned} \quad (5)$$

In general, when we deal with protoplanetary disks, the diffusivities η_O and η_A increase with larger grains due to aforementioned analyses.

3. NUMERICAL SETUP

This letter studies PPDs that are subject to the impact of spatial distribution of dust grains. For brevity, we refer the readers to Wang et al. (2018) (WBG19 hereafter) for the details in (1) the methods of global full MHD simulations combined with consistent thermochemistry and ray-tracing radiation, (2) the initial conditions. For the boundary conditions, we inherited the setups in WBG19 except for the toroidal field above the disk region (viz. inside the wind region) at the inner radial boundary: we set $B_\phi = -B_r|_{t=0}$ (the initial value of r component) to suppress magnetic instabilities there. (note that the magnetization here is ~ 20 times WBG19 in terms of absolute magnetic pressures and stresses. The plasma β at midplane is 2×10^4 , 5 times smaller than WBG19) Other hydrodynamic and field components are identical to WBG19.

The dust grains are still treated as single-sized carbonaceous grains co-moving with the gas. The size is either $a_{\text{gr}} = 5$ (Model S) or $a_{\text{gr}} = 10^{-2} \mu\text{m}$ (Model L). On the other hand, the variation of their properties is reflected by adjusting their total abundance so that the total geometric cross-section of dust grains per hydrogen nucleus, $\sigma_{\text{gr}}/\text{H}$, matches the value obtained from the dust evolution calculation (bottom panel of Figure 1), as a function of the cylindrical radius R to the central star. The basic properties of our fiducial model (Model S) are summarized in Table 1. Maximum $\sigma_{\text{gr}}/\text{H}$ is $8 \times 10^{-23} \text{ cm}^2$ in both models, which equals to 7×10^{-6} in dust to gas mass ratio in Model S, and 1.4×10^{-4} in Model L, if we take the average density of a single grain as 2.25 g cm^3 . We note that the grains

Table 1. Properties of Model S (§3)

Item	Value
Radial domain	$1 \text{ AU} \leq r \leq 100 \text{ AU}$
Latitudinal domain	$0.035 \leq \theta \leq 3.107$
Resolution	$N_{\log r} = 384, N_{\theta} = 192$
Stellar mass	$1.0 M_{\odot}$
$M_{\text{disk}} (1 \text{ AU} \leq r \leq 100 \text{ AU})$	$0.10 M_{\odot}$
Initial mid-plane density	$8.03 \times 10^{14} (R/\text{AU})^{-2.2218} m_p \text{ cm}^{-3}$
Initial mid-plane plasma β	10^4
Initial mid-plane temperature	$305 (R/\text{AU})^{-0.57} \text{ K}$
Artificial heating profile	$305 (R/\text{AU})^{-0.57} \text{ K}$
Luminosities [photon s^{-1}]	
7 eV (“soft” FUV)	4.5×10^{42}
12 eV (LW)	1.6×10^{40}
3 keV (X-ray)	1.1×10^{38}
Initial abundances [$n_{\text{X}}/n_{\text{H}}$]	
H ₂	0.5
He	0.1
H ₂ O	1.8×10^{-4}
CO	1.4×10^{-4}
S	2.8×10^{-5}
SiO	1.7×10^{-6}
Dust/PAH properties	
a_{gr}	5
$\sigma_{\text{gr}}/\text{H}$	Variable (§3)

in the two models have the same total geometric cross section but couple to magnetic fields differently. The grains in Model L have a grain-neutral collision coefficient $\langle \sigma v \rangle_{\text{gr}}$ that is two orders of magnitude larger than the grains in Model S. The behavior of very small grains are actually similar to ions, as the Hall parameter of ions is approximately $\beta_i \approx 3.3 \times 10^{-3} (B_G/n_{15})$. For larger charged grains, smaller β_{gr} indicates weaker coupling to magnetic fields, which means that grains are more prone to frequent collision with neutrals.

4. RESULTS

Figure 2 summarizes the main point of this paper: the impact of grain sizes on radial ionization structure and how rings and gaps form from it. In Model S, where grains have the same size as WBG19 (5 PAH), the variation of dust number density yields some effects on surface density beyond 10 AU, and there are no apparent features associated with $\sigma_{\text{gr}}/\text{H}$ bumps at 13 AU and 28 AU. In Model L, the location of rings and gaps at these two snow lines are very close to Hu et al. (2019). From the non-ideal MHD point of view, the simulations prove that number density variation of

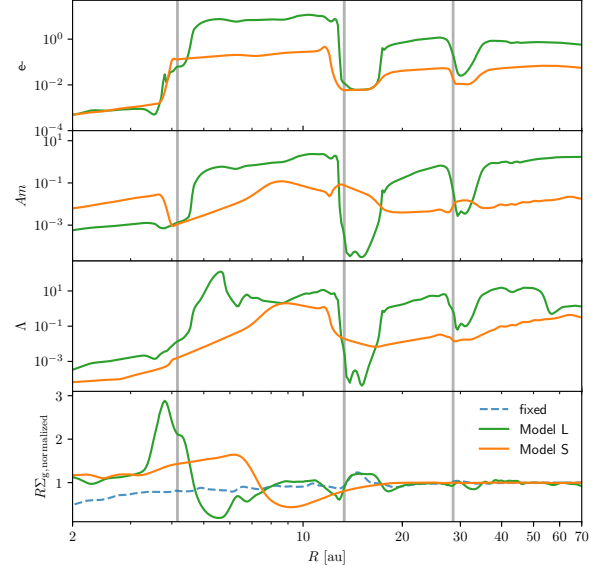


Figure 2. From top to bottom: electron density (cm^{-3}), Ambipolar Elsasser number Am , Ohmic Elsasser number Λ and normalized surface density. Green lines are from Model L ($1 \times 10^{-6} \text{ cm}$ grain) and orange lines are Model S. The blue dashed lines in the bottom panels (“fixed”) is the disk model with fixed temperature and ionization structure from Hu et al. (2019). The location of snow/sintering lines are marked with gray vertical lines.

PAH-scaled grains has sub-linear impacts on magnetic diffusivities. The two middle panels shows the Elsasser numbers of both Ohmic resistivity and Ambipolar diffusion of Model S, which have mild change at 13 AU and 28 AU snow lines, comparing to order of magnitude jump of $\sigma_{\text{gr}}/\text{H}$. The diffusivity profiles of Model L reflect the $\sigma_{\text{gr}}/\text{H}$ structures quite well. Diffusion strength increases up to 4 orders of magnitude at those two snow lines, where the total $\sigma_{\text{gr}}/\text{H}$ rises by about 10 times.

After 1500 orbits at the innermost radius, the overall disk structure of both simulations reaches a quasi-steady phase, as shown in Figure 3. In what follows, we recognize the disk surface as the location of wind launching, i.e., where both v_z and v_R are positive and poloidal velocity $\sqrt{v_z^2 + v_R^2}$ is more than 50% of local sound speed. Above the wind base, the Alfvén surface is where the velocity in the poloidal plane equals to the poloidal Alfvén velocity $v_{A,p} = \sqrt{(v_z^2 + v_R^2)/4\pi\rho}$.

4.1. Thermochemistry

Both models exhibit vertical profiles in thermochemistry at each radius that are qualitatively similar to Wang et al. (2018): a relatively warm magnetized wind above the dense, relatively cold disk. Quantitative properties of these vertical profiles, nonetheless, are sensi-

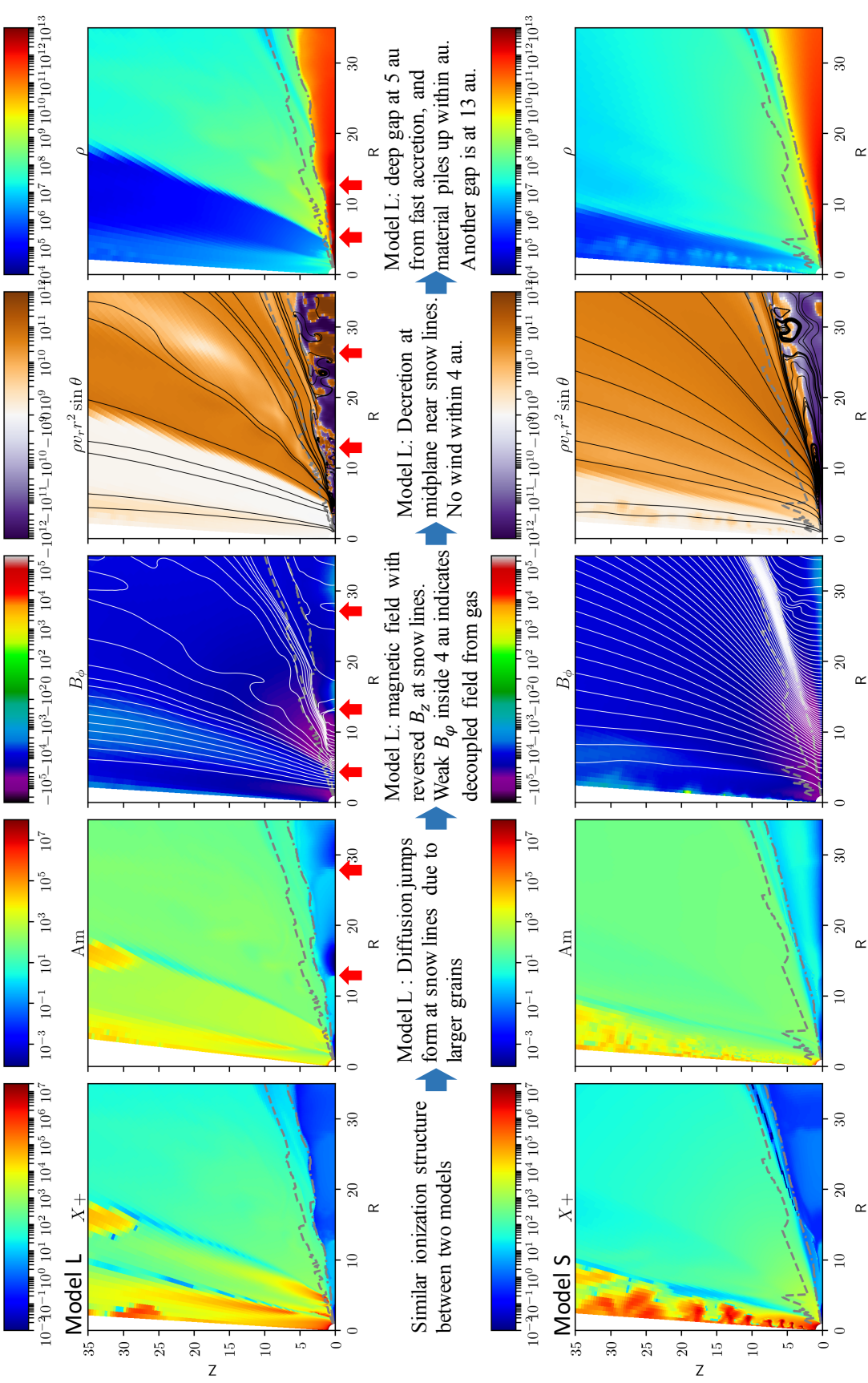


Figure 3. Meridional slices of Model L (Upper) and Model S (Lower), averaged from $t = 1496$ yr to $t = 1500$ yr with $dt = 1.0$ yr (except the X^+ panel is a snapshot at $t = 1500$ yr). From left to right we illustrate the physical process of substructure formation, especially in Model L: number density of the summation of all positive charge carriers except Gr^+ ; Elsasser number of Ambipolar diffusion; toroidal field strength in code units, with white lines as magnetic field lines; effective mass flux and stream lines of gas velocity (black solid lines); gas density measured in number density of H atom (cm^{-3}). The gray dashed lines indicate poloidal Alfvén surface, and the gray dash-dotted lines are wind base/disk surface.

tively modulated by the radial variations in dust effective cross section. For Model S, because of the enhanced adsorption efficiency of charged particles at smaller dust sizes [Draine & Sutin \(1987\)](#), throughout most radial ranges, the overall abundances of charge-carrying species (including free electrons, ions, but not Gr^\pm since they have little contribution to conductivity in Model L) are lower than Model L. Near the innermost snowline of H_2O ($R \simeq 4$ AU), Model L exhibits significant fluctuation due to mixture of materials that brings uneven relative abundance of dusts. Note that the co-moving dusts do not change its initial radial distribution significantly.

Because the dust-dust neutralization process ($\text{Gr}^+ + \text{Gr}^- \rightarrow 2\text{Gr}$) is relatively slow, charged grains (Gr^\pm) become the predominant charge carriers in the mid-plane in both models (similar to [Xu & Bai 2016](#); [Wang et al. 2018](#)). As indicated by Eq. 2, charged grains behave like ions at small sizes in terms of $\langle \sigma v \rangle$ —whether a free charge is carried by an ion or a charged tiny grain, it contributes similarly to the conductivity (thus magnetic diffusivity). Therefore, the radial variation in diffusivity (indicated by the Elsasser numbers) in Model S is not as intensive as the variation in dust effective cross section. In contrast, Model L exhibits much lower Elsasser numbers at those radii where the effective cross sections are high, since the $a_{\text{gr}} = 10^{-6}$ cm grains do not contribute appreciably to the components of tensorial conductivity due to frequent collision with neutrals (eq.3,4). This difference induced by dust sizes are signified by its impact on MHD diffusivities, which will be elaborated in what follows.

4.2. Dynamics and Kinematics of Accretions and Winds

In a (quasi-)steady accretion disk, the accretion is driven by (1) the radial gradient of $T_{R\phi}$ (the $R\phi$ component of the magnetic stress tensor), and (2) the difference of the $T_{z\phi}$ stress between the top and bottom disk surfaces, namely,

$$\frac{\dot{M}_{\text{acc}} v_K}{4\pi} = \frac{\partial}{\partial R} \left(R^2 \int_{\text{bottom}}^{\text{top}} T_{R\phi} dz \right) + R^2 [T_{z\phi}]_{\text{bottom}}^{\text{top}}. \quad (6)$$

The first term in eq. 6 resembles a radial stress and can be characterized by the equivalent Shakura-Sunyaev α parameter,

$$\alpha = \left[\int_{\text{bottom}}^{\text{top}} p_{\text{gas}} dz \right]^{-1} \times \int_{\text{bottom}}^{\text{top}} T_{R\phi} dz. \quad (7)$$

Quantities associated with these components of accretion rates are summarized in Figure 4 and 5. The accretion rate \dot{M}_{acc} is integrated mass flux below the wind

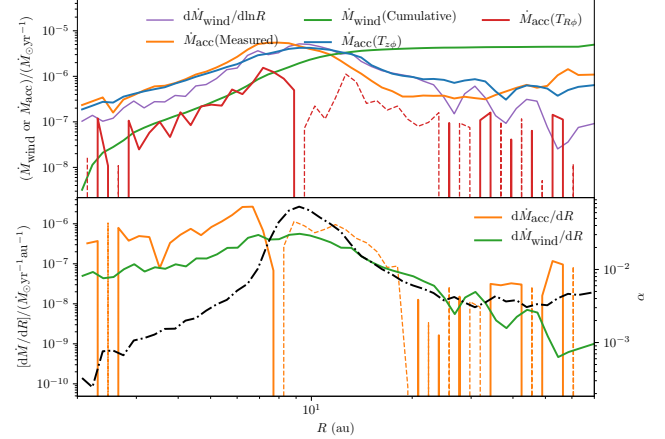


Figure 4. One-dimensional radial profiles on disk’s mass flux, in the case of Model S. In the upper panel are measured accretion rate in disk (\dot{M}_{acc} (Measured)), wind loss rate (both cumulative and per $\ln R$), and estimated accretion rate caused by $R\phi$ and $z\phi$ Maxwell stress. Lower panel shows the accretion rate variation by distance to star and wind loss rate per unit radii. The Shakura-Sunyaev α parameter for radial angular momentum transport is also presented in black dashed-dot line on the right y axis.

base, i.e., dot-dashed gray lines in Figure 3. The wind loss rate \dot{M}_{wind} is vertical mass flux (ρv_z) measured at wind base. Similar to [Hu et al. \(2019\)](#) and [Wang et al. \(2018\)](#), the $T_{z\phi}$ stress (viz. the stress that drives wind) is the predominant factor of accretion in both Models.

The second term in eq. 6 represents the contribution of wind stresses. Along a field line, the cylindrical radius of wind base R_{wb} and the radius where it intersects with Alfvén surface R_A is related to the ratio of wind loss rate and steady accretion rate caused by wind torque:

$$\dot{M}_{\text{acc,wind}} = 2 \left[\left(\frac{R_A}{R_{\text{wb}}} \right)^2 - 1 \right] \left(\frac{d\dot{M}_{\text{wind}}}{d \ln R} \right). \quad (8)$$

The ratio R_A/R_{wb} is referred to as “magnetic lever arm”. For example, based on the field lines presented in the lower panel of Figure 3, the value of lever arm is about 1.4 within 10 AU; hence, the local accretion rate should be 1.92 times of $d\dot{M}_{\text{wind}}/d \ln R$ in Model S.

4.2.1. Model S

For Model S, the lower panel of Figure 3 observes steady accretion below $\sim 2/3$ the height of wind base, and outflow dominates above that. Both velocity streamlines and magnetic field lines in Figure 3 show apparent wind launching inside 10 AU, while beyond 10 AU the outgoing flux is almost parallel to the disk surface. The strengths of both poloidal and toroidal field components are significantly weaker than $R < 15$ AU.

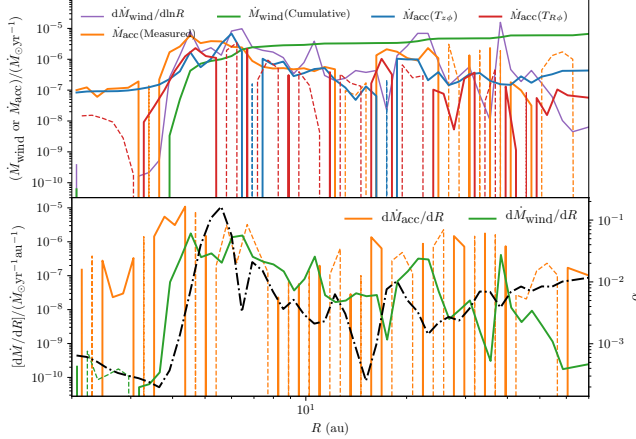


Figure 5. Same as Figure 4 but for Model L

Therefore, the wind torque is weaker at the outer region, expecting a lower accretion rate and slower evolution for the substructures.

Inside the disk, the Elsasser numbers Am and Λ have no apparent feature observed at the 13 AU and 28 AU snow lines due to the effects elaborated in §4.1. Radial differentiation of accretion and wind-launching rates are most distinguishable near $R \sim 7$ AU, at which the fields concentrate and the accretion rate peaks ($\dot{M}_{acc} \simeq 5 \times 10^{-6} M_{\odot} \text{ yr}^{-1}$). This profile is clearly reflected by the resulting surface density profile (Figure 2) and the rates of wind launching (lower panel, Figure 4). The accretion driven by the $T_{z\phi}$ stress is always about one order of magnitude higher than the contribution of the $T_{R\phi}$ stress. In fact, the radial gradient of the $T_{R\phi}$ stress drives a layer of *decretion* rather than accretion in the range $10 \text{ AU} \lesssim R \lesssim 22 \text{ AU}$, indicating that the toroidal field decreases faster than R^{-2} in this radial range. Within 10 AU, the accretion rate is about twice as much as $d\dot{M}_{wind}/d\ln R$, which is consistent with the magnetic lever arm argument (eq. 8).

4.2.2. Model L

The outcomes of our simulation are quite different in Model L. At radii slightly above the 4 AU, 13 AU and 28 AU snow lines (where σ_{gr}/H rises significantly), both Am and Λ decrease to yield stronger diffusion (see also §4.1). Such features in magnetic diffusion modulate the way that the disk accretes. Figure 3 presents an obvious characteristics of Model L: the absence of wind and wind-driven accretion at radii $R \lesssim 4$ AU. Immediately outside this snowline radius, concentration of magnetic fields causes excessive mass transfer rates in both wind and accretion, causing a gap at $R \sim 5$ AU. Qualitatively similar features exemplify themselves at snow lines at 13 AU and 28 AU. Overall, the mass transport is much

more chaotic than Model S; wind and accretion structures below the Alfvén surface are not laminar. Similar to Hu et al. (2019), accretion and decretion (flowing outwards but the streamlines not reaching super-Alfvénic) regions are associated by poloidal field loops at mid-plane, as shown in the upper middle panel of Figure 3. From 12 to 15 AU, the averaged net accretion flow in the disk is even negative (i.e. net decretion); similar decretion was reported in Hu et al. (2019) at approximately the same location. Such differentiation exemplifies itself at the $R \simeq 28$ AU snowline. Around the local density minima associated with these snow lines, the equivalent viscous α reaches its local maxima, as the magnetic and fluid fluxes are more turbulent there than the neighbors. Beyond 6 AU, radial stress ($T_{R\phi}$) induced accretion starts to play an equally important role as wind ($T_{z\phi}$).

4.2.3. Not to launch a wind

One of the most distinctive feature of Model L is the absence of wind within 4 AU (Figure.3). We can understand this by analysing vertical accretion structure. Since the mass accretion rate is $\dot{m}_{acc} = -2\pi R \int_{bot}^{up} \rho v_R dz$, we can rewrite Eq. 6 in derivative form so we can calculate accretion flux at different vertical layers:

$$-\rho v_R = \frac{2}{Rv_K} \frac{\partial}{\partial R} (R^2 T_{R\phi}) + \frac{2R}{v_K} \frac{\partial T_{z\phi}}{\partial z} \quad (9)$$

We show vertical slice of mass flux and Maxwell stress in Model L at $R = 3$ AU and $R = 7$ AU in Figure.6, with $R = 7$ AU being the reference. At $R = 7$ AU the disk has a "regular" structure as seen in the mass flux and density panel in Figure.3. This is reflected in the vertical accretion analysis. Accretion is confined within a relatively thin sheet (a little more than one scale height) in the midplane, and above that we see decretion and wind. Both $T_{R\phi}$ and $T_{z\phi}$ drive accretion at midplane. At disk surface is the competition between $T_{R\phi}$ driven decretion and $T_{z\phi}$ accretion and the winner is $T_{R\phi}$. At the wind region, R component of wind is related to $T_{z\phi}$ and it dominates over $T_{R\phi}$ that tends to drag wind back to central star. The combination is the predicted flux at leftmost panels of Figure.6. Mass flux at both wind region and disk region is well predicted by stress calculation.

At this point we can understand how not to launch wind at $R = 3$ AU. Contribution from $T_{R\phi}$ and $T_{z\phi}$ cancels out when $z/R > 0.2$. Magnetic field lines threading the disk surface need to be bent both vertically (opening angle outward) and azimuthally (strong ϕ component) to lift material up. In Figure.3 we find the field lines are almost vertical, respect to disk surface within 4 AU in Model L.

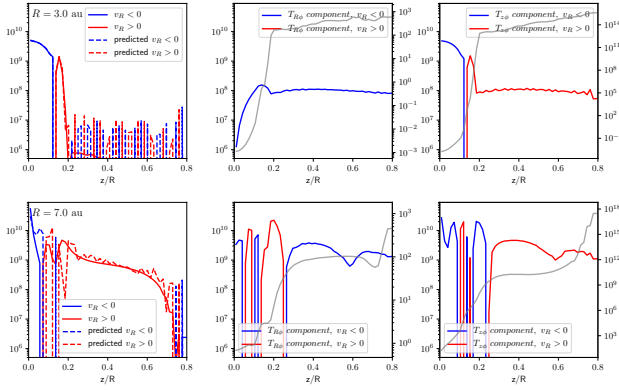


Figure 6. Vertical profiles of local mass flux [in code units] at $R = 3$ AU. Blue and red colors indicate accretion and decretion/outflow, respectively. In the left panels, solid lines are measured directly from the simulation, while dashed curves are values predicted from magnetic stress, i.e., right side of Eq.9. Middle panels show the predicted mass flux contributed by $R\phi$ magnetic stress, and the right panels show contribution from $z\phi$ stress. The gray solid line in the middle panel shows same vertical profile of Ambipolar Elsasser number Am with right side y-axis, and in the right panel is Ohmic Elsasser number Λ .

5. DISCUSSION AND SUMMARY

This work discusses the impact of grain sizes on the non-ideal MHD accretion processes and subsequently formation of sub-structures in PPDs. Dust grains are categorized into two populations by size, which have qualitatively different levels of impact onto the sub-structure formation in PPDs. PAH-sized grains behave as ions when charged, thus do not correspond to significant non-ideal MHD diffusivity features. Larger (\gtrsim sub-micron) charged grains interact with neutrals with much bigger cross-section, whose number density is related to diffusivities directly. Physical processes that affect the radial distribution of larger grains (e.g., by snow lines) lead to the formation of rings and gaps via the radial variation of accretion rates (dominating) and wind launching rates (secondary importance).

Structure formation due to the jump of the non-ideal MHD accretion rates would lose efficiency wherever PAHs are much more abundant (in terms of effective cross-section) than sub-micron-sized grains. Therefore, the ubiquity of PPD sub-structures suggests that PAHs could be relatively rare in absence of planet-induced structure formation. This inference accords with the lack of PAH signals detected in low mass embedded YSOs (Geers et al. 2009). In the dense regions where

the temperature is relatively low, PAHs tend to freeze out and be retained by the surfaces of larger grains (e.g., Anderson et al. 2017).

Our non-ideal MHD simulations have connected ionization chemistry (especially dust-related processes) to sub-structure formation through accretion dynamics, but they still have a few caveats. The variation in grain sizes feeds back to the rings’ locations via snow lines, as the severity of “traffic jams” in accretion, in turn, depends on dust size and location. Therefore, the majority of dust grains redistributed by snow lines are not necessarily the group that dominates sub-structure formation via magnetic diffusion. In our current models, dust grains are still single-sized species co-moving with gas, which is still insufficient to account for the dust redistribution for the complete loop of feedbacks in the sub-structure formation. Radial drift alone is not efficient even for the larger grains in Model L; those grains that concentrate rapidly at pressure maxima cannot dominate the balance of ionization as they are much less in number density. Such concentration of dust, in the meantime, can also result in more fragmentation hence transfer mass in dust rings to smaller grains. Thus, a complete multi-species dust model needs to be implemented with multiple dust sizes. A viable method is to use the two-population (big and small) recipe of dust that involves coagulation and fragmentation processes for the transfer of mass between these two populations (e.g. Birnstiel et al. 2012; Tamfal et al. 2018; Kanagawa et al. 2018). In addition, particle-based dust grain models are critical to study the vertical distribution of the two-population dusts for their sedimentation, settling, and PAH freezing processes, which are likely to concentrate the grains near the equatorial plane and make the interior of disk more susceptible to the sizes of grains.

ACKNOWLEDGEMENTS

X.H. and Z.Z. acknowledge support from the National Aeronautics and Space Administration through the Astrophysics Theory Program with Grant No. NNX17AK40G. Simulations are carried out with the support from the Texas Advanced Computing Center (TACC) at The University of Texas at Austin through XSEDE grant TG-AST130002. L.W. acknowledges support from Center for Computational Astrophysics of Flatiron Institute. S.O. is supported by JSPS KAKENHI Grant Numbers JP16K17661, JP18H05438, and JP19K03926

REFERENCES

ALMA Partnership, Brogan, C. L., Pérez, L. M., et al. 2015, *ApJ*, 808, L3, doi: [10.1088/2041-8205/808/1/L3](https://doi.org/10.1088/2041-8205/808/1/L3)

Anderson, D. E., Bergin, E. A., Blake, G. A., et al. 2017, *ApJ*, 845, 13, doi: [10.3847/1538-4357/aa7da1](https://doi.org/10.3847/1538-4357/aa7da1)

- Bai, X.-N. 2011a, *ApJ*, 739, 51,
doi: [10.1088/0004-637X/739/1/51](https://doi.org/10.1088/0004-637X/739/1/51)
- . 2011b, *ApJ*, 739, 50, doi: [10.1088/0004-637X/739/1/50](https://doi.org/10.1088/0004-637X/739/1/50)
- . 2014, *ApJ*, 791, 72, doi: [10.1088/0004-637X/791/1/72](https://doi.org/10.1088/0004-637X/791/1/72)
- Bai, X.-N., & Stone, J. M. 2017, *ApJ*, 836, 46,
doi: [10.3847/1538-4357/836/1/46](https://doi.org/10.3847/1538-4357/836/1/46)
- Béthune, W., Lesur, G., & Ferreira, J. 2017, *A&A*, 600,
A75, doi: [10.1051/0004-6361/201630056](https://doi.org/10.1051/0004-6361/201630056)
- Birnstiel, T., Klahr, H., & Ercolano, B. 2012, *A&A*, 539,
A148, doi: [10.1051/0004-6361/201118136](https://doi.org/10.1051/0004-6361/201118136)
- Draine, B. T. 2011, *Physics of the Interstellar and
Intergalactic Medium*
- Draine, B. T., & Sutin, B. 1987, *ApJ*, 320, 803,
doi: [10.1086/165596](https://doi.org/10.1086/165596)
- Geers, V. C., van Dishoeck, E. F., Pontoppidan, K. M.,
et al. 2009, *A&A*, 495, 837,
doi: [10.1051/0004-6361:200811001](https://doi.org/10.1051/0004-6361:200811001)
- Gonzalez, J. F., Laibe, G., & Maddison, S. T. 2017,
MNRAS, 467, 1984, doi: [10.1093/mnras/stx016](https://doi.org/10.1093/mnras/stx016)
- Hu, X., Zhu, Z., Okuzumi, S., et al. 2019, arXiv e-prints,
arXiv:1904.08899. <https://arxiv.org/abs/1904.08899>
- Huang, J., Andrews, S. M., Dullemond, C. P., et al. 2018,
ApJ, 869, L42, doi: [10.3847/2041-8213/aaf740](https://doi.org/10.3847/2041-8213/aaf740)
- Kanagawa, K. D., Muto, T., Okuzumi, S., et al. 2018, *ApJ*,
868, 48, doi: [10.3847/1538-4357/aae837](https://doi.org/10.3847/1538-4357/aae837)
- Long, F., Pinilla, P., Herczeg, G. J., et al. 2018, *ApJ*, 869,
17, doi: [10.3847/1538-4357/aae8e1](https://doi.org/10.3847/1538-4357/aae8e1)
- Okuzumi, S., Momose, M., Sirono, S.-i., Kobayashi, H., &
Tanaka, H. 2016, *ApJ*, 821, 82,
doi: [10.3847/0004-637X/821/2/82](https://doi.org/10.3847/0004-637X/821/2/82)
- Okuzumi, S., & Tazaki, R. 2019, *ApJ*, 878, 132,
doi: [10.3847/1538-4357/ab204d](https://doi.org/10.3847/1538-4357/ab204d)
- Suriano, S. S., Li, Z.-Y., Krasnopolsky, R., & Shang, H.
2017, *MNRAS*, 468, 3850, doi: [10.1093/mnras/stx735](https://doi.org/10.1093/mnras/stx735)
- . 2018, *MNRAS*, 477, 1239, doi: [10.1093/mnras/sty717](https://doi.org/10.1093/mnras/sty717)
- Suriano, S. S., Li, Z.-Y., Krasnopolsky, R., Suzuki, T. K.,
& Shang, H. 2019, *MNRAS*, 484, 107,
doi: [10.1093/mnras/sty3502](https://doi.org/10.1093/mnras/sty3502)
- Tamfal, T., Drażkowska, J., Mayer, L., & Surville, C. 2018,
ApJ, 863, 97, doi: [10.3847/1538-4357/aad1f4](https://doi.org/10.3847/1538-4357/aad1f4)
- Wang, L., Bai, X.-N., & Goodman, J. 2018, arXiv e-prints,
arXiv:1810.12330. <https://arxiv.org/abs/1810.12330>
- Wang, L., & Goodman, J. 2017, *ApJ*, 847, 11,
doi: [10.3847/1538-4357/aa8726](https://doi.org/10.3847/1538-4357/aa8726)
- Wardle, M. 2007, *Ap&SS*, 311, 35,
doi: [10.1007/s10509-007-9575-8](https://doi.org/10.1007/s10509-007-9575-8)
- Xu, R., & Bai, X.-N. 2016, *ApJ*, 819, 68,
doi: [10.3847/0004-637X/819/1/68](https://doi.org/10.3847/0004-637X/819/1/68)
- Zhang, K., Blake, G. A., & Bergin, E. A. 2015, *ApJ*, 806,
L7, doi: [10.1088/2041-8205/806/1/L7](https://doi.org/10.1088/2041-8205/806/1/L7)